THE AMERICAN SOCIETY OF MECHANICAL ENGINEERS
345 E. 47 St., New York, N.Y. 10017



86-GT-188



# The Off-Design Performance of a Low Pressure Turbine Cascade

**H. P. HODSON**
**R. G. DOMINY**
Whittle Laboratory,
University of Cambridge,
U.K.

ABSTRACT

The ability of a given blade profile to operate over a wide range of conditions is often of the utmost importance. This paper reports the off-design performance of a low pressure turbine rotor root section in a linear cascade. Data were obtained using pneumatic probes and surface flow visualisation. The effects of incidence (+9, 0, -20 deg.), Reynolds No. (1.5, 2.9, $6.0 \times 10^5$), pitch-chord ratio (0.46, 0.56, 0.69) and inlet boundary layer thickness (0.011, 0.022 $\delta^*/C$) are discussed. Particular attention is paid to the three-dimensionality of the flow field. Significant differences in the detail of the flow occur over the range of operating conditions investigated. It is found that the production of new secondary loss is greatest at the lower Reynolds numbers, positive incidence and the higher pitch-chord ratios.

NOMENCLATURE

| | |
|---|---|
| C | chord |
| Cx | axial chord |
| h | span |
| M | Mach Number |
| p | static pressure |
| Po | stagnation pressure |
| R | reattachment line |
| Re | Reynolds Number |
| s | pitch |
| S | separation line |
| x | axial distance |
| y | pitchwise distance |
| Y | total pressure loss coefficient $(P_{01} - P_0)/(P_{04} - p_4)$ |
| z | spanwise distance |
| $\beta$ | pitchwise flow angle (from axial) |
| $\delta^*$ | boundary layer displacement thickness |
| $\theta$ | boundary layer momentum thickness |
| $\rho$ | density |

Suffices

| | |
|---|---|
| $\infty$ | free stream |
| 1 | inlet free stream |
| 2 | traverse plane |
| 2s | downstream isentropic |
| 3 | pitchwise mixed out |
| 4 | downstream infinity (i.e. pitch and spanwise mixed out) |
| s | suction side |
| p | pressure side |
| 0-6 | number of separation/reattachment line |

INTRODUCTION

During the preliminary design or redesign of an axial flow turbine, various methods of performance estimation (e.g. [1]-[4]) are employed. These or similar methods are inevitably based upon correlations and it is therefore recognised that they cannot replace either more detailed design methods or test data. Nevertheless, they are often used to investigate the directions that future aerodynamic developments should take and it is under such circumstances that correlations of this kind are least reliable. Indeed, as it should be, it is often stated by authors that their methods are only applicable to turbines which contain "well behaved" blades.

In the case of low pressure turbines, it can be difficult to arrive at a design which will contain such profiles. Near the rotor hub, for example, the common desire to produce a uniform work distribution can lead to a root section with relatively little overall expansion. A companion paper [5] describes a detailed cascade investigation of the three-dimensional performance of such a profile when operating at its design condition. In a turbine, a profile will operate over a large range of conditions yet, there is very little data available from such turbines concerning the primary and particularly the secondary flow.

This paper presents a study of the off-design performance of a low pressure turbine rotor root section in cascade. Particular attention is given to the three-dimensional apsects of the flow. The effects of incidence, Reynolds number, inlet boundary layer thickness and pitch-chord ratio are described.

EXPERIMENTAL APPARATUS

The experimental results were obtained in the Transonic Cascade Facility of the Whittle Laboratory,

Presented at the International Gas Turbine Conference and Exhibit
Dusseldorf, West Germany—June 8-12, 1986

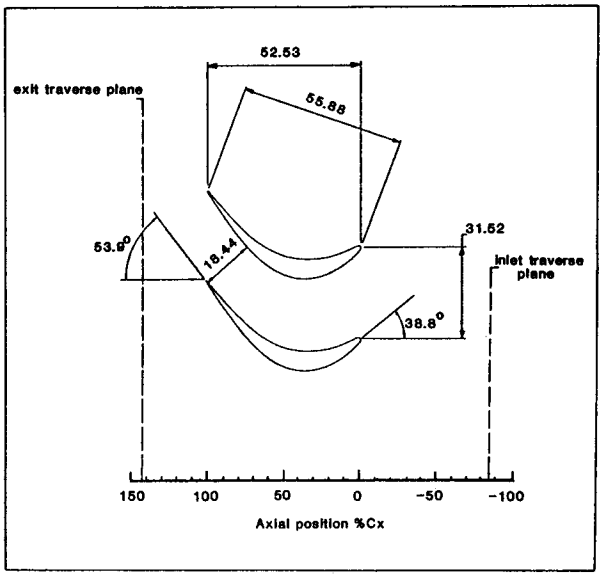


**Fig. 1 Cascade : Side view of a single passage**

Cambridge. This is a closed circuit tunnel in which the Mach number ($M_{2S} < 1.4$) and the Reynolds number ($0.3 \times 10^5 < Re_{2S} \leq 20 \times 10^5$) can be varied independently.

The cascade consisted of six blades which exhausted into a large plenum chamber. The rotor root section is shown schematically in Fig. 1. It was designed to operate at an inlet angle of 38.8°, an exit angle of approximately 54° from the axial direction at an exit Mach number of 0.7 and a chord based exit Reynolds number of $2.9 \times 10^5$ . The cascade was also designed to accommodate the effects of stream tube height variation by specifying a 6 percent flare of the blade span with a linear variation in aspect ratio between the inlet and exit planes of the cascade. Further details can be found in Table 1 and ref. [5].

The central passage of the cascade was instrumented with static pressure tappings at mid-span. Inlet static pressure tappings were located 0.86 Cx upstream of the leading edge plane. A pitot was placed at the same position. The inlet stagnation temperature (15-35 °C) was measured using a thermocouple which was placed within the ducting upstream of the working section.

Two further probes have been employed during the current investigation. The first consisted of a fixed-drection 5-hole 60 deg. conical probe with an overall diameter of 2mm. This was used to traverse the cascade exit flow at 142%Cx. The second probe was a flattened pitot (0.14x1.16mm) which was used to traverse the inlet endwall boundary layer at -86%Cx. The facility is provided with a fully automated computer controlled data aquisition system. The estimated maximum experimental inaccuracies associated with the various measurements and cascade settings are given in Table 2.

Visualisations of the surface flows were obtained using a mixture of fluorescent powder and silicone oil. The mixture was applied to the surfaces prior to the passage of air through the cascade. The viscosity of the mixture and the duration of the experiments were such that the patterns were unaffected by the starting and stopping of the tunnel.

TABLE 1: BLADE DESIGN, CASCADE GEOMETRY AND OPERATING CONDITIONS

| | |
|---|---|
| No. of Blades | 6 |
| Chord, C (mm) | 55.88 |
| Axial Chord, Cx (mm) | 52.53 |
| Inlet Aspect Ratio, $h_1/C$ | 1.715 |
| Exit Aspect Ratio, $h_2/C$ | 1.818 |
| Pitch-Chord ratio, s/C | 0.564 |
| Pitch-Axial Chord ratio, s/Cx | 0.600 |
| Design Inlet Angle (deg. from axial) | 38.8 |
| Design Exit Angle (deg. from axial) | -53.9 |
| $Cos^{-1}(O/s)$ | -54.2 |
| Stagger Angle (deg. from axial) | -19.6 |
| Throat-Pitch ratio, O/s | 0.585 |
| Leading Edge radius-chord ratio | 0.016 |
| Isentropic Exit Mach number | 0.71 |
| Isentropic Exit Reynolds Number | $2.9 \times 10^5$ |

## RESULTS AND DISCUSSION

The three-dimensional aerodynamic performance of the cascade has been determined over a range of operating conditions. The nominal design point of the cascade is given in Table 1. Unless otherwise stated, the parameters in a given test are identical to those given in the table with the exception of that (e.g. Reynolds number) which is under investigation.

Table 3 summarises the traverses made through the inlet boundary layer 86%Cx upstream of the leading edge plane of the cascade. The upstream potential influence of the cascade is negligible at this location. The results show that the inlet boundary layer is turbulent at all of the conditions tested with a displacement thickness to chord ratio ($\delta^*/C$) of approximately 0.01 except in the case of the deliberately (using trips) thickened inlet boundary layer. All boundary layer parameters have been determined using the compressible form of the appropriate expression or integral with the assumption that the static pressure is uniform and equal to the value at the wall.

In the following discussion, the results of area exit traverses are presented. Due to physical constraints, these data were only obtained between 2.0 and 50.0 percent of the span. Therefore, the average values which are given do not include the loss etc., which are associated with the fluid (including the exit endwall boundary layer) which is to be found between the wall and 2.0 percent of the span.

All of the average properties, whether area or pitchwise averaged, have been determined using a constant area mixing calculation in which the inviscid adiabatic equations for the conservation of mass, energy and momentum are applied. The difference between the mixed-out quantities and the simple mass averaged values ranged from 7 to 15 percent of the total measured loss, depending upon the non-uniformity of the velocity field which in turn was a function of the operating conditions.

Table 4 provides a breakdown of the exit based loss coefficient into those associated with the inlet boundary layer, albeit at 86%Cx upstream of the cascade, the profile loss at the mid-span of the blade and the remainder, the so-called net secondary loss. It is of course recognised that the latter is a concept born out of a need for a convenient method of identification of the losses rather than an understanding of the flow.

TABLE 2: ESTIMATE OF EXPERIMENTAL ACCURACY

| | | |
|---|---|---|
| Linear Position | +/- 0.01 mm | |
| Inlet Flow Angle | +/- 0.2 deg. | |
| Exit Flow Angle | +/- 0.4 deg. | |
| Stagnation Pressure (5 hole probe) | +/- 0.003 | $\times(P_{04} - p_4)$ |
| Stagnation Pressure (All Pitots) | +/- 0.001 | |
| Static Pressure (5 hole probe) | +/- 0.005 | |
| Static Pressure (surface tappings) | +/- 0.001 | |

TABLE 3: INLET BOUNDARY LAYERS

| Test Condition | $\delta^*/C$ | $\theta/C$ | $\delta^*/B$ |
|---|---|---|---|
| Design | 0.0108 | 0.0075 | 1.44 |
| Re2 = $1.5 \times 10^5$ | 0.0093 | 0.0065 | 1.44 |
| Re2 = $6.0 \times 10^5$ | 0.0097 | 0.0068 | 1.44 |
| +8.6 degrees incidence | 0.0108 | 0.0075 | 1.44 |
| -20.3 degrees incidence | 0.0108 | 0.0075 | 1.44 |
| s/C = 0.459 | 0.0108 | 0.0075 | 1.44 |
| s/C = 0.688 | 0.0108 | 0.0075 | 1.44 |
| Thickened inlet b.l. | 0.0221 | 0.0163 | 1.36 |

The sections which follow concentrate on the major differences which occur in the structure of the flow at the various test conditions.

Design Conditions:

A description of the development of the primary and secondary flow fields within the cascade at its design point has already been presented in a companion paper [5]. However, for completeness and as an aid to the interpretation of the data presented here, those results are summarised below.

Fig. 2 is taken from ref. [5]. It contains an interpretation of the endwall and suction surface flow visualisation. The separation lines (S1s and S1p) and saddle point associated with the roll-up of the inlet boundary layer, the separation line (S3) and reattachment line (R3) of the corner vortex and the separation line (S4) of the passage vortex are all shown. The closed separation bubble near the leading edge of the suction surface is caused by an overspeed which is known [6] to have little overall effect upon the suction surface boundary layer which undergoes laminar separation (S5), transition and reattachment (R5) near the trailing edge. The flow visualisation also shows that the suction side leg of the horse-shoe vortex (S2s) interacts with this closed separation bubble. In doing so, some of the high loss fluid is fed into the separation bubble while the rest is convected with the vortex towards the trailing edge. Although not shown in the illustration, a closed separation bubble also exists on the pressure side of the blade close to the leading edge. This is caused by the diffusion which follows the acceleration of the flow around the leading edge. In practice, it seems that the pressure side and suction side leading edge bubbles have little overall effect upon the development of the secondary flows and losses at zero incidence.

Some of the above mentioned features can be traced downstream to the traverse plane located at 142% Cx (Fig. 3). The secondary velocities in the figure were calculated by projecting the velocity vectors onto a plane which was perpendicular to the mixed out flow direction. In this and in other figures, the contours of secondary vorticity, which were calculated by finite differentiation of the secondary velocities, have been used to identify the centres of the various vortices. The centres of the passage vortex and its associated loss core are indicated in Fig. 3. They are coincident. The locations of the corner vortex (identified using the loss contours) and that which contains the trailing shed vorticity are also shown. The suction side leg of the horse-shoe vortex could not

TABLE 4: MIXED OUT TRAVERSE RESULTS

| Condition | Total Loss Coeff. | Mixing Loss Coeff. | Inlet Loss Coeff. | Mid-span Loss Coeff. | Net Secondary Loss Coeff. | Axial Velocity Density Ratio | Exit Flow Angle (deg.) |
|---|---|---|---|---|---|---|---|
| Design | 0.0639 | 0.0059 | 0.0110 | 0.0270 | 0.0259 | 0.917 | 54.1 |
| Re2 = $1.5 \times 10^5$ | 0.0715 | 0.0053 | 0.0093 | 0.0354 | 0.0268 | 0.916 | 54.3 |
| Re2 = $6.0 \times 10^5$ | 0.0594 | 0.0070 | 0.0101 | 0.0263 | 0.0230 | 0.907 | 54.1 |
| +8.6 deg. incid. | 0.1007 | 0.0148 | 0.0149 | 0.0498 | 0.0360 | 0.923 | 54.1 |
| -20.3 deg. incid. | 0.0810 | 0.0026 | 0.0075 | 0.0598 | 0.0137 | 0.907 | 53.5 |
| s/c = 0.459 | 0.0625 | 0.0041 | 0.0104 | 0.0344 | 0.0177 | 0.929 | 54.2 |
| s/c = 0.688 | 0.0680 | 0.0084 | 0.0105 | 0.0278 | 0.0297 | 0.935 | 53.8 |
| Thick inlet b.l. | 0.0764 | 0.0055 | 0.0239 | 0.0280 | 0.0245 | 0.928 | 53.9 |

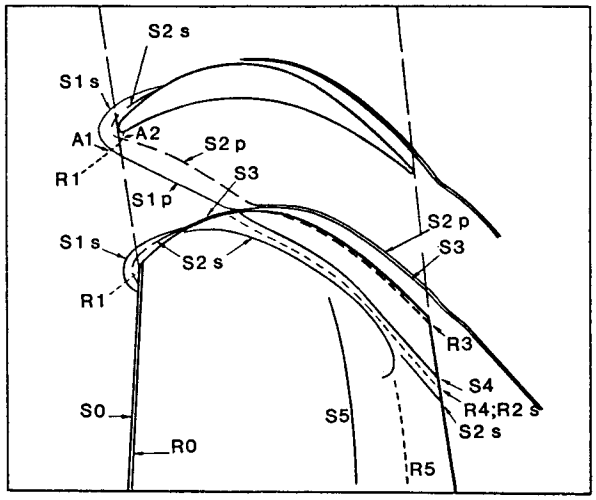


Fig. 2 Suction surface and end wall flow visualisation [5]

be indentified even though its path could be traced using the surface flow visualisation.

Variation with Reynolds number :

At a Reynolds number of $1.5 \times 10^5$, which is one half of the design value, the flow visualisation revealed that the suction surface boundary layer separates near 68% Cx with reattachment just prior to the trailing edge. The isentropic Mach number distributions of Fig. 4 show how the bubble grows in extent as the Reynolds number is reduced from the design value. A consequence of the now extensive separation is that the interaction between the secondary flow and the suction surface boundary layer fluid is greater than at the design condition. The suction surface flow visualisation (Fig. 5a), for example, revealed that the separation line of the suction side leg of the horse-shoe vortex disappeared as it encountered the separated flow. This

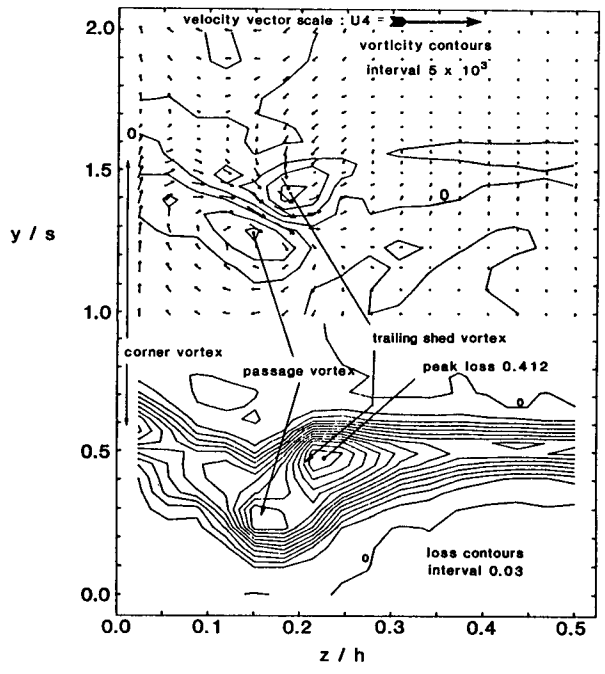


Fig. 3 Total pressure loss coefficient contours, vorticity contours and secondary velocity vectors. Design Condition

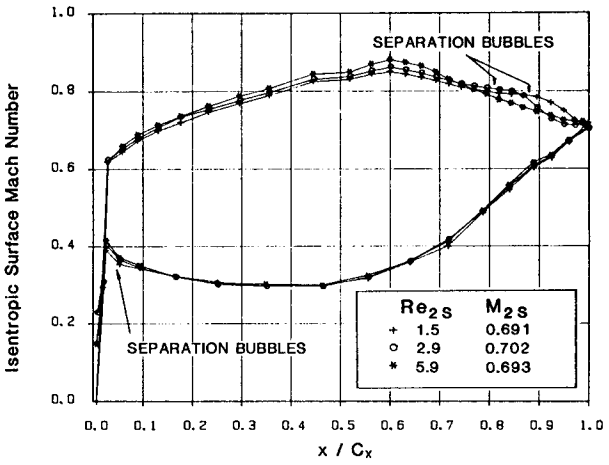


**Fig. 4 Blade surface Mach Number distributions : Reynolds Number variation**

increase in the strength of the interaction is thought to be related to the relatively low static pressure in the bubble as well as the unsteadiness and mixing which would accompany a large separation, phenomena which would also explain the absence of a constant pressure region over the upstream portion of the separation bubble.

Fig. 6 contains the results of the exit area traverse at the lowest Reynolds number. It shows that the details within the wake and secondary flow regions are less well defined than at the design condition (Fig. 3). This is partly due to the increased interaction between the secondary and suction surface flow which was indicated by the flow visualisation. However, reducing the Reynolds number will also increase the rate of decay of the wake and secondary flow regions and this is thought to be mainly responsible. The secondary velocity vectors are also shown in fig. 6. Due to the apparent increase in the rate of decay, they are smaller than at the design value. The secondary vorticity contours reveal that the peak strengths of the passage and the trailing shed vortices are 75% of the values at the design condition. As a consequence, the distortion of the centre line of the wake has reduced. It also appears that the roll up of the trailing shed vorticity is less complete than at the design condition. However, the locations of peak vorticity and, therefore, the vortex centres are virtually unchanged.

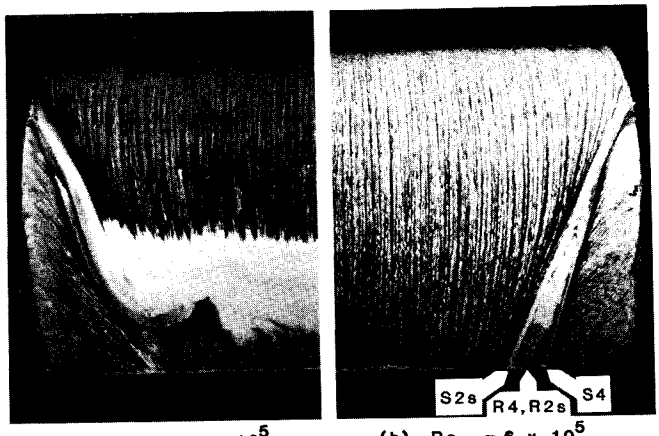


**Fig. 5 Suction surface flow visualisation**

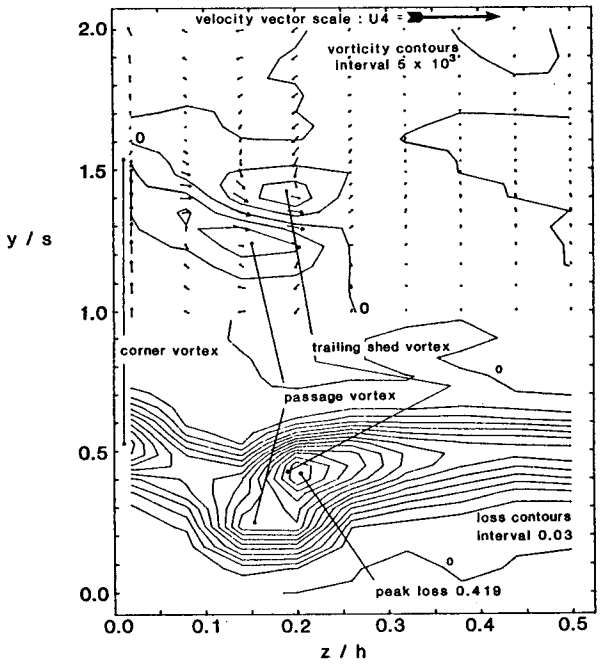


**Fig. 6 Total pressure loss coefficient contours, vorticity contours and secondary velocity vectors. Low Reynolds Number**

At a Reynolds number of $6.0 \times 10^5$, which is twice that of the design value, transition to turbulent flow is sufficiently complete to prevent the separation of the suction surface boundary. The surface oil flow patterns are shown in Fig. 5b. The absence of the suction surface separation means that the three dimensionality of the suction surface flow is reduced and that the separation line (S2s) which is associated with the suction side leg of the horse shoe vortex is clearly visible over the rear of the surface. Otherwise, the development of the surface flow is very similar to that observed at the lower Reynolds numbers.

The absence of a back surface separation and the higher Reynolds number result in more clearly defined wake and secondary flows (Fig. 7). Likewise, the magnitudes of the secondary velocities and therefore vorticities are greater. The peak vorticity within the passage vortex, for example, is increased by approximately 35%. The distortion of the centre line of the wake is therefore greater although again, the positions of the passage and trailing shed vortices are unchanged. Fig. 7 also reveals that there are now three rather than two loss peaks near 20% span and that they all reach similar values, which was not the case at the lower Reynolds numbers. The innermost peak is thought to come from the fluid within the suction side leg of the horse shoe vortex and from the reattachment zone (R4/R2) between this and the separation line of the passage vortex. Relatively little vorticity is associated with this loss peak. That which exists is of opposite sign to that of the passage vortex. The middle loss peak is centred on the counter rotating vortex which contains the trailing shed vorticity and the outermost is the passage vortex.

The spanwise variations of the pitchwise mixed out stagnation pressure loss and yaw angle obtained at the three Reynolds numbers are plotted in Fig. 8. As might be expected from the previous discussion regarding the state of the suction surface boundary layer, the midspan loss decreases with increasing Reynolds number. Similarly, the extent of the constant loss and yaw angle region over the central portion of the blade increases as the Reynolds number is

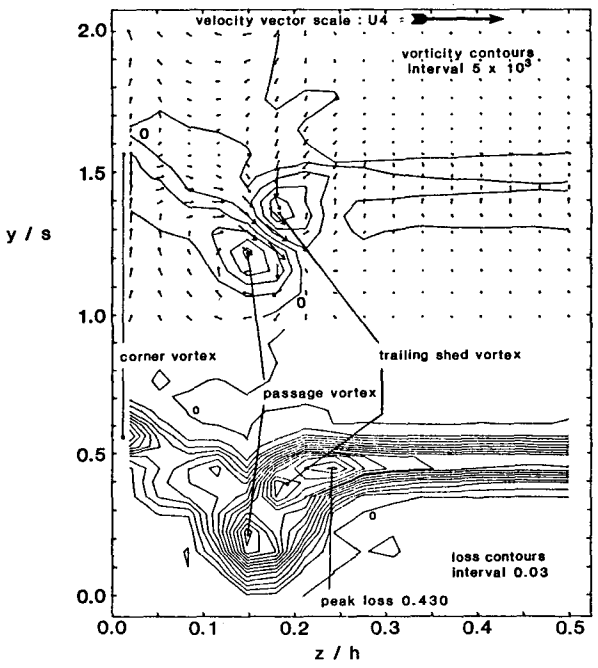


**Fig. 7 Total pressure loss coefficient contours, vorticity contours and secondary velocity vectors. High Reynolds Number**

increased and the three-dimensionality of the surface flow is reduced. Near the endwall, the amount of overturning and by implication the nature of the growth of the new end wall boundary layer appears to be independent of Reynolds number. However, the variation in flow angle near the centre of the passage vortices, in particular the amount of underturning, is Reynolds number dependent. This is a consequence of the changing strengths of the passage and trailing shed vortices as the Reynolds number is varied.

It has already been noted (Fig. 8) that the mid-span loss reduces with increasing Reynolds number. Table 4 shows that the same is true of the total loss and the net secondary loss. The latter is derived by subtracting the inlet and mid-span loss from the total.

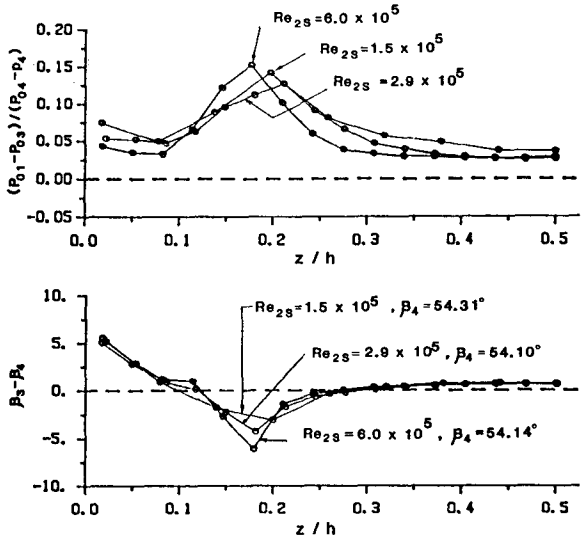


**Fig. 8 Mixed out pitchwise flow angle and stagnation pressure loss : Reynolds Number variation**

The validity of such a calculation has already been questioned. Nevertheless, the indicated trends are undoubtedly valid. These are, that reducing the Reynolds number increases the mid-span and the net secondary losses. However the proportions by which these increase are very different. The mid-span or "profile" loss for example decreases by 25 percent as the Reynolds number is quadrupled while the net secondary loss decreases by 14 percent. This difference arises because the nature of the suction surface boundary layer changes significantly over the range of Reynolds numbers investigated whereas the secondary flow patterns are virtually unchanged, apart from the interaction of the suction side leg of the horse-shoe vortex with the suction surface boundary layer. In several correlations (e.g. [4]), the secondary loss is assumed to be proportional to $Re^{-0.2}$ as is the profile loss. In the case of the present cascade no simple power law can be used to describe the variations observed. The overall variation in secondary loss from the highest to the lowest Reynolds number is however much less than this simple relationship implies although the variation from the design to the highest value does imply a proportionality to $Re^{-0.15}$.

Variation with Incidence :

The performance of the cascade was investigated at two inlet flow angles other than the design value. These angles, which are equivalent to incidences of -20.3 and +8.6 degrees, were chosen to represent the extremes which might be encountered by the profile during operation in a turbine. The mid-span isentropic Mach number distributions which correspond to these inlet flow angles are plotted in Fig. 9. It can be seen that the inlet flow angle has a significant effect upon the pressure distribution over much of the blade surface. At positive incidence, the pressure surface diffusion has almost vanished. The flow visualisation showed that as a result, there is no pressure surface leading edge separation bubble. Data (unpublished) similar to those in reference [6] suggest that the pressure side boundary layer remains laminar up to the trailing edge. On the suction surface, operation at positive incidence significantly increases in the size of the leading edge overspeed. Behind the separation bubble which follows this overspeed, there is a region of almost constant static pressure within which the reattached, presumably turbulent, boundary layer

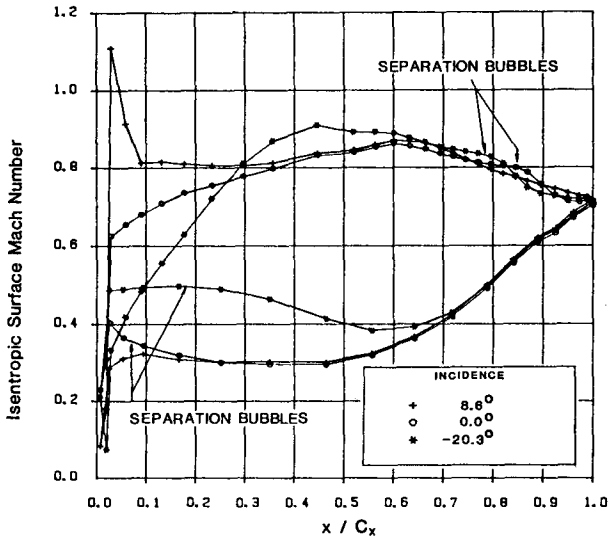


**Fig. 9 Blade surface Mach Number distributions : Incidence variation**

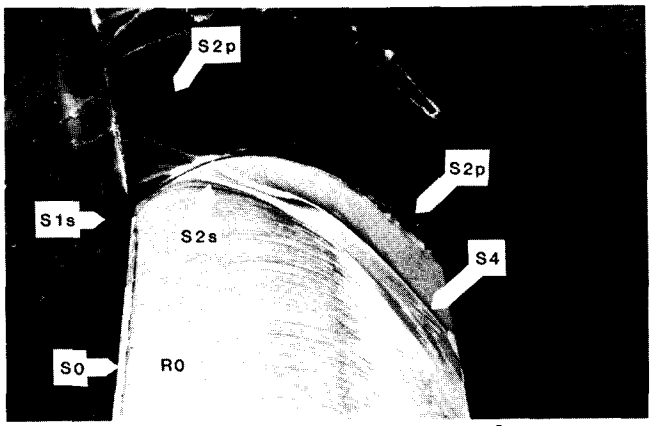


**Fig. 10 Surface flow visualisation : +8.6° incidence**

develops. Therefore, there is no back surface separation.

Fig. 10 shows a perspective view of the suction surface and endwall oil flow visualisation patterns obtained at positive incidence. The secondary separation line S2s-S2p associated with the upstream movement of fluid near the leading edge into the horseshoe vortex is clearly visible. This was not the case at the design condition. The appearance and disappearance of a second separation line associated with the formation of the leading edge vortex has been addressed in reference [5]. The difference is presumably a consequence of the greater leading edge loading at positive incidence as indeed must be the greater rate of downwash of fluid onto the suction surface. The primary separation line of the pressure-side leg of the horse-shoe vortex (S1p), for example, meets the suction surface at 25% Cx rather than at the design condition value of 33% Cx. However. the saddle points associated with the primary and secondary separation lines of the horse shoe vortex have moved very little. This result must be contrasted with that of reference [7] which revealed a large shift in the position of the saddle point as the incidence of the flow onto an H.P. rotor was increased.

Fig. 10 also shows that increasing the incidence onto the blades increases the three dimensionality of the suction surface oil flow patterns. The separation lines S4 and S2s associated with the passage and suction side horseshoe vortex are displaced towards midspan and between them, lies a larger reattachment zone. The absence of any truly spanwise flow on the rear of the suction surface is due to the continuous attachment of the blade surface boundary layer. The speckled flow visualisation on the back surface is merely a result of the reduced shear stress which follows peak suction. It does not signify separation, but the difference between this picture and that of Fig. 5b does suggest that the suction surface boundary layer is not fully turbulent. Unpublished data for simliar profiles, which includes transition measurements, support this view point.

Further evidence of the increased three dimensionality of the flow field is contained in Fig. 11. Compared to the design case, the strengths of the passage and counter rotating vortices have increased significantly. For example, the peak vorticity within the passage vortex has increased by 65% and the counter rotating vortex which contains the trailing shed vorticity has increased in strength by approximately 35%. As a result of the greater downwash of fluid onto the suction surface, the centres of the vortices are now closer to mid-span. The centre of the passage vortex is coincident with its associated loss peak

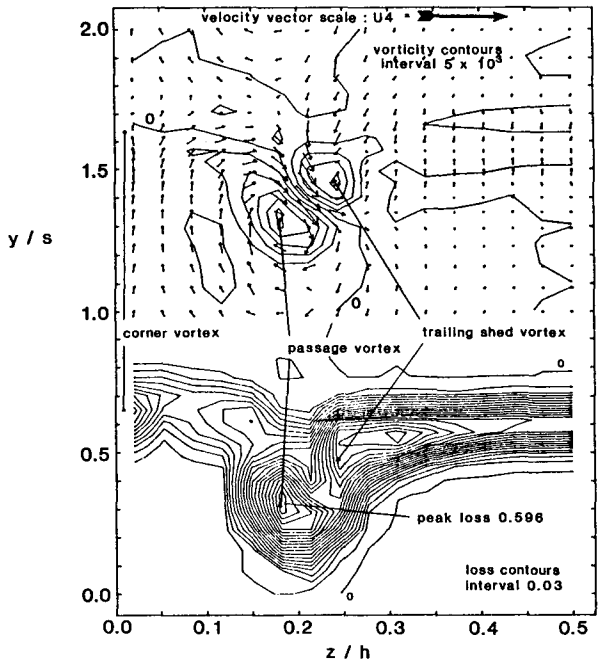


**Fig.11 Total pressure loss coefficient contours, vorticity contours and secondary velocity vectors. Positive (8.6 deg) incidence**

which is itself of the same magnitude as the peak which lies nearest mid-span. The height of the loss peaks were similarly matched at the highest Reynolds number, when the back surface boundary layer was also attatched. The rate of entrainment of fluid into the wake region appears to be greater than at the design condition. This is thought to be due to the increased strength of the vortices, and in particular the passage vortex.

At approximately 20 degrees of negative incidence, the Mach number distribution of Fig. 9 shows that the loading becomes negative up to 10%Cx. The now continuous acceleration over the leading half of the suction surface means that the suction surface boundary layer remains laminar until following peak suction, it separates, undergoes transition and finally reattachment near to the trailing edge. Thus, the suction surface boundary layer is similar to that which occurs at the design condition. On the pressure surface, however, there is a region of almost constant static pressure between 3 and 25%Cx, which is indicative of a long separation bubble.

The extent of the pressure side separation bubble

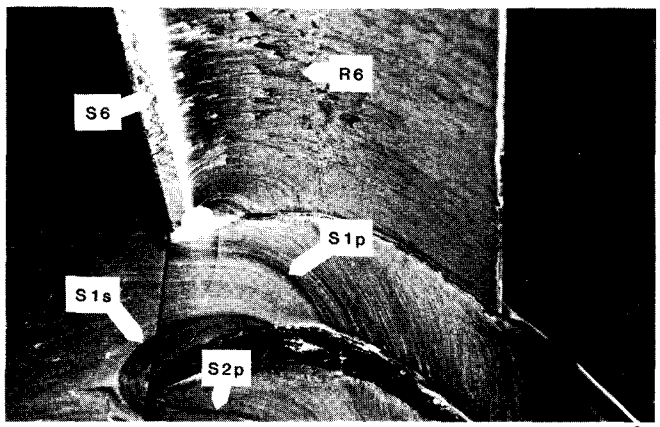


**Fig. 12 Pressure side surface flow visualisation : -20°**

can be seen in Fig. 12, which contains a perspective view of the pressure surface and endwall flow patterns. Near mid-span, the bubble extends from approximately 5% to 45% Cx. In the pressure surface endwall corner, the flow is highly three-dimensional, with reversed flow occuring on both the blade and endwall surfaces. The positions of the separation and reattachment lines are indicated. This separated flow region is so large that the mixing which occurs between the separated flow and the free stream results in stagnation pressures which, downstream of the cascade, are everywhere less than the inlet free stream value. This is illustrated by Fig. 13, which contains some of the data obtained during a mid-span pitchwise traverse. Whether this phenomena should be termed "negative stalling" is, however, unclear since an embedded and attached boundary layer develops over the rear half of the pressure surface. A further consequence of operating at negative incidence can be seen in the flow visualisation picture of Fig. 12. The saddle point associated with the primary separation line of the horse-shoe vortex now lies on the suction side of the blade.

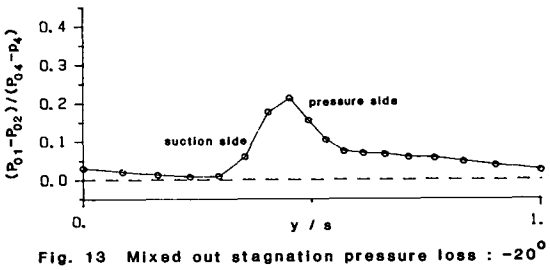


**Fig. 13 Mixed out stagnation pressure loss : -20°**

Because the fluid experiences less turning at negative incidence as it passes through the cascade, the secondary flow is reduced. This is shown by Fig. 14, which contains some of the exit traverse results. Whether the separation of the pressure surface flow and its subsequent mixing with the mainstream also contribute to the reduction is unclear. It is also apparent that the strength of the passage vortex is much less than that of the trailing shed vortex. Estimates of the vorticity indicate that the trailing shed vortex has a strength which is 50% of its value at the design incidence. The strength of the passage vortex, which is only just identifiable, is reduced to 25% of its value at the design conditions. This difference in the relative strengths of the two vortices and the overall level of secondary flows are thought to explain the appearance of only one loss peak other than the corner vortex, near 15% span.

The spanwise variation of loss and flow angle derived from the exit traverses at the three inlet flow angles are plotted in Fig. 15. At mid-span the loss is lowest at the design incidence. At positive, incidence it is greater because the suction surface boundary layer is turbulent over much of its surface length. At -20.3 degrees of incidence the increase is due to the large pressure side separation. As was the case with the Reynolds number variation, the extent of the regions of constant loss and turning decrease and the variation in yaw angle increases with increasing secondary flow. In contrast to the effects of changing the Reynolds number, the overturning near the wall is also dependent upon the flow conditions. This is due to the very different secondary flows which result from the modifications made to the loading distribution as the inlet flow angle is altered.

Table 4 provides a breakdown of the total loss. The apparent variation in inlet loss with inlet flow angle is a result of converting the measured loss at

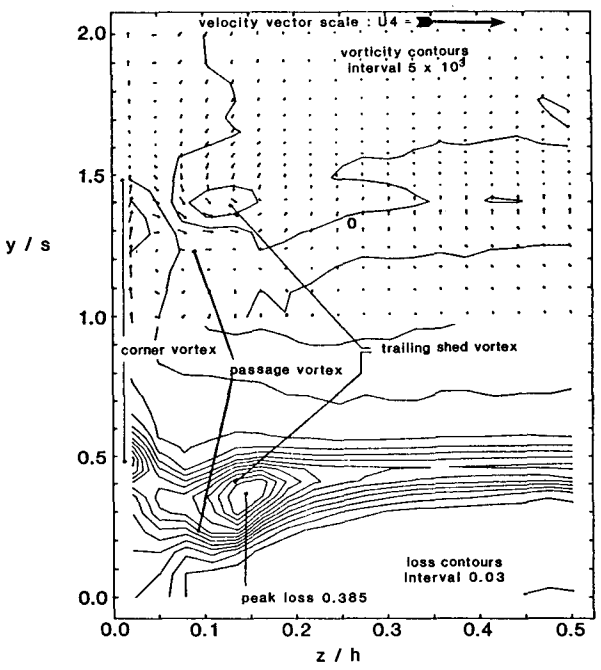


**Fig.14 Total pressure loss coefficient contours, vorticity contours and secondary velocity vectors. Negative (-20.3 deg) incidence**

inlet into an exit-based coefficient. Subtracting this and the mid-span value of loss from the total reveals, not surprisingly, that the net secondary loss is greatest at positive incidence (50% higher) and least at negative incidence, where it is one half of the value at the design condition. Application of the correlation of Craig and Cox [4] reveals that the measured values are approximately one half of those predicted. A comparison between the cascade correlation of Dunham [8] and the turbine correlation of Dunham and Came [3] shows that such a difference is not unreasonable. The relative changes are, however, accurately predicted by reference [4]. In contrast, reference [3] and, indeed, the method of Ainley and Mathieson [1] upon which that of reference [3] is based predict that for this particular cascade the net secondary loss should decrease, albeit only slightly, with increasing incidence over the range investigated.

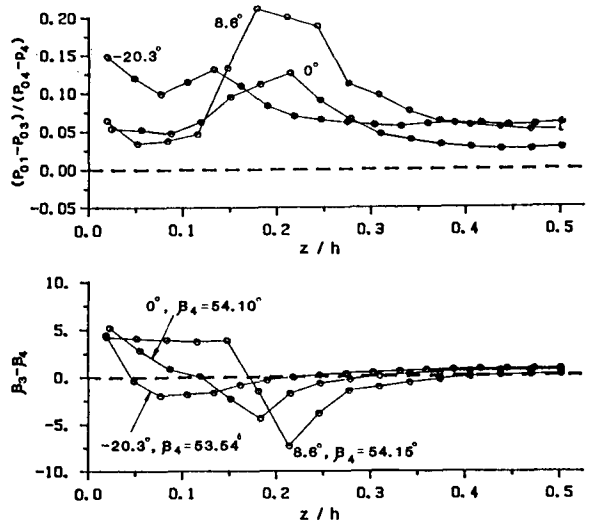


**Fig. 15 Mixed out pitchwise flow angle and stagnation pressure loss : incidence variation**

Variation of Pitch-Chord ratio:

An examination of secondary loss correlations (e.g. [1]-[4]) shows that it is unclear whether or not pitch-chord ratio is a parameter upon which secondary losses are dependent. Craig and Cox [4], for example, predict a significant dependence while the correlation of Dunham [8], for no other reason than a lack of data does not contain the pitch-chord ratio as an independent variable.

Given this uncertainty, it was decided to investigate the effects of pitch-chord ratio upon the performance of the current cascade. The changes in pitch-chord ratio (i.e. +22%, -18% s/C) necessitated a change in the number of blades in the cascade. The details are given in Table 5. For each pitch a different stagger was selected in order to maintain the same exit flow angle as predicted by a coupled inviscid boundary layer computation. The measured flow angles show that this requirement was largely satisfied.

TABLE 5: CASCADE GEOMETRIES FOR MODIFIED PITCH

| | Design | +22% s/C | -18% s/C |
|---|---|---|---|
| Pitch-Chord Ratio | 0.564 | 0.688 | 0.459 |
| Pitch-Axial Chord Ratio | 0.600 | 0.732 | 0.492 |
| Stagger | -19.6° | -18.2° | -20.6° |
| No. of blades in cascade | 6 | 5 | 7 |

Fig. 16 contains the isentropic mid-span Mach number distributions measured at the three pitch-chord ratios investigated. Increasing the pitch chord ratio increases the blade loading. At the largest pitch, the leading edge overspeed, which was too short to be detected by static pressure measurements at the design point, has increased in surface length. Presumably this is a result of the greater stagger although the increased loading may also contribute. The effect of this enlarged overspeed upon the suction surface boundary layer is slight however, since separation and turbulent reattachment again occur on the back surface.

The increase in pitch-chord ratio has a marked effect upon the three dimensionality of the flow. Fig. 17 shows a view of the suction surface oil-flow patterns. The leading edge separation bubble is just visible. At the rear of the surface, the interaction of the suction side horseshoe vortex with the shortened separation bubble is greater than at the design pitch. It may also be significant that the secondary separation line associated with the leading edge horseshoe vortex was clearly visible in the endwall flow patterns and that the only other condition at which this was so was at +8.6 degrees of incidence.

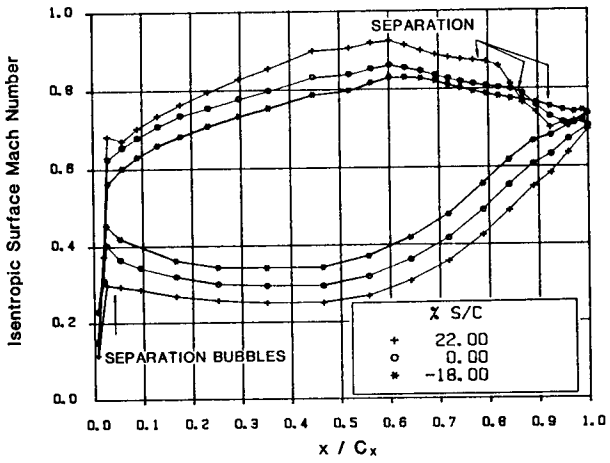


**Fig. 16 Blade surface Mach Number distributions Pitch-Chord ratio variation**

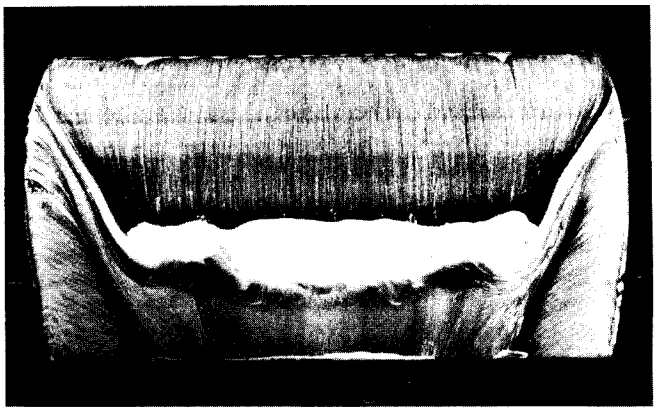

**Fig. 17 Suction surface flow visualisation : +22% s / C**

Fig. 18 contains the results of the exit traverse at the increased pitch-chord ratio. Like the measurements at the highest Reynolds number (Fig. 7) three loss peaks are visible between 20 and 30% span. That nearest the endwall corresponds to the centre of the passage vortex the strength of which, like that of the adjacent vortex of opposite rotation, is greater than at the design value. As a result of the increased secondary flow, the vortices also lie nearer mid-span. At positive incidence, where the loading was also greater, a similar shift was observered.

In general, reducing the pitch chord ratio has the opposite effect to that observed above. The Mach number distribution (Fig. 16), for example, shows that the blade loading is reduced. However, the low base pressure and apparent lack of any reattachment zone suggest that the back surface separation is no longer closed. The flow visualisation results also suggested that this was in fact the case.

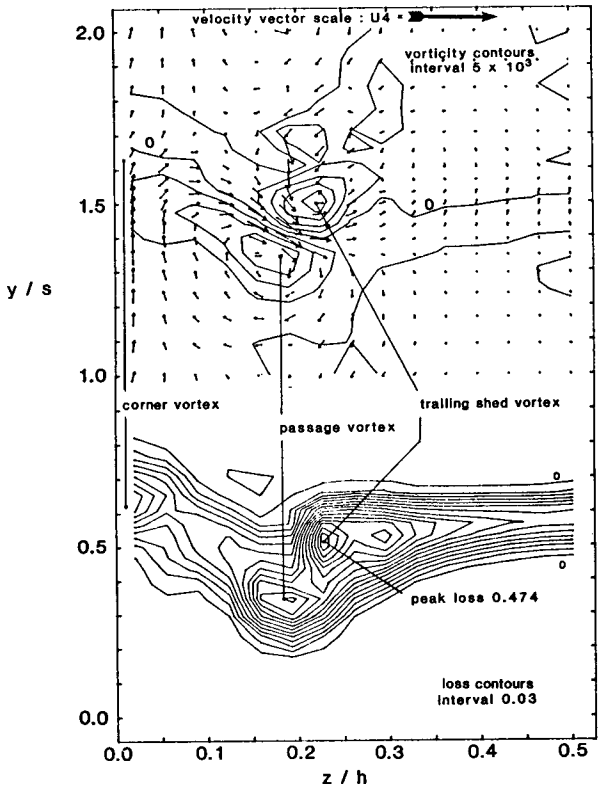


**Fig.18 Total pressure loss coefficient contours, vorticity contours and secondary velocity vectors. Increased Pitch-Chord Ratio**

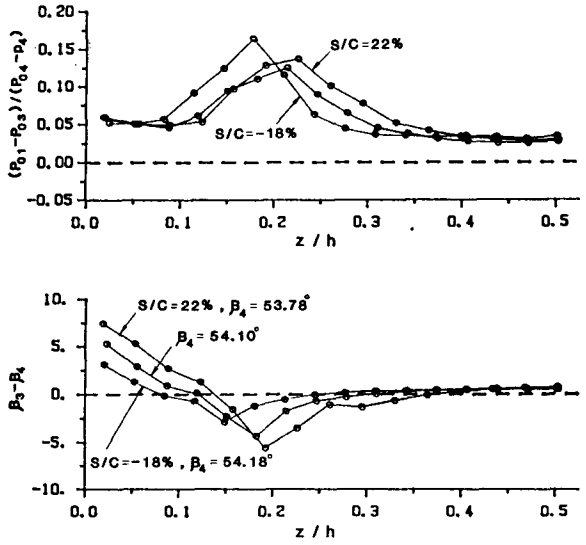


**Fig. 19 Mixed out pitchwise flow angle and stagnation pressure loss : Pitch-Chord variation**

Fig. 19 summarises the effects of pitch-chord ratio upon the exit flow field. The amount of overturning close to the endwall does indeed depend upon the pitch-chord ratio as does the position and magnitude of the maximum underturning all of which are related to the strength of the secondary flow. Similarly, the position of the loss peak which is associated with the passage vortex moves towards mid-span as the pitch-chord ratio is raised. All of these changes imply that the secondary flow is not independent of the pitch-chord ratio.

Table 4 again provides a breakdown of the losses at exit from the cascade. In terms of the pitch-chord ratio variation, the midspan loss is greatest at the lowest ratio since gross separation of the suction surface boundary layer has occurred. Increasing the pitch-chord ratio above the design value appears to have little effect upon the mid-span loss. In contrast, the net secondary loss increases with increasing pitch. For example, the relative increase from the lowest to the highest pitch-chord ratio is equal to 70%.

Variation of Inlet Boundary Layer Thickness :

The various correlations which exist relate the net secondary loss through a cascade to such parameters as deflection, Reynolds number and aspect ratio. Some, but not all, also attempt to relate the increase in loss to that contained in the upstream endwall boundary layer but such a dependency is only valid if the mechansims of horse-shoe vortex formation generate a significant amount of entropy. Various investigations, e.g. [7],[9] and [10], which map the generation of loss through a cascade, suggest that this is not the case. In the present cascade, the thickness of the inlet boundary layer was doubled in a further attempt to determine the extent to which the generation of new loss is dependent upon that which exists at inlet. Table 3 contains details of the thicker boundary layer.

The results of the surface flow visualisation were very similar to those obtained at the design condition. The only significant difference was in the distance between the primary separation line of the horseshoe vortex and the leading edge, which reduced from 5.5 to 3.5 leading edge radii as the thickness was doubled. The results of the exit area traverse are plotted in Fig. 20. This shows that a much greater proportion of the flow area is occupied by high loss fluid. The loss peak associated with the passage vortex is only just visible and the centre of the passage vortex, which is identified by the position of peak vorticity, lies further from the endwall and suction surface. The magnitudes of the secondary velocity vectors associated with the trailing-shed vorticity are similar to those observed in the case of the thinner inlet boundary layer. The peak strength of the passage vortex is however reduced. Given the decrease in the maximum value of vorticity within the inlet boundary layer, this might be expected.

A comparison of the spanwise variation of loss and yaw angle at the different inlet boundary layer thicknesses is provided in Fig. 21. It shows the greater loss and overturning near the endwall in the case of the thicker inlet boundary layer as well as the more gradual variation in under and over turning which is presumably due to the changed distribution of

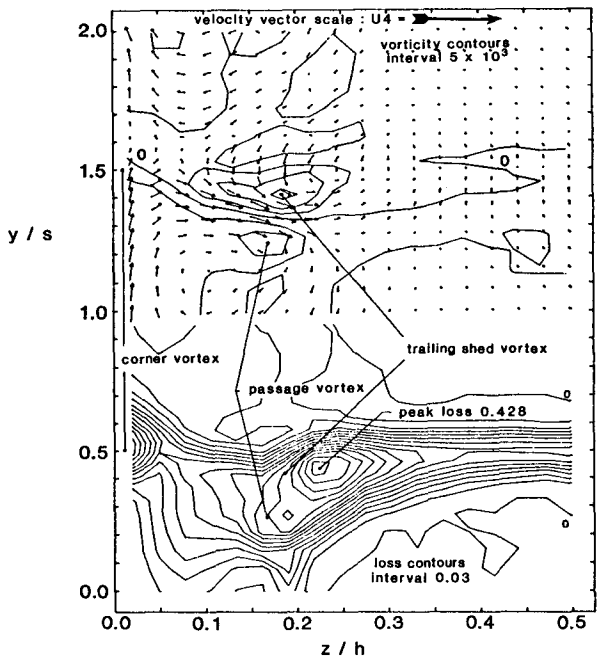


**Fig.20 Total pressure loss coefficient contours, vorticity contours and secondary velocity vectors. Thick Inlet Boundary Layer**

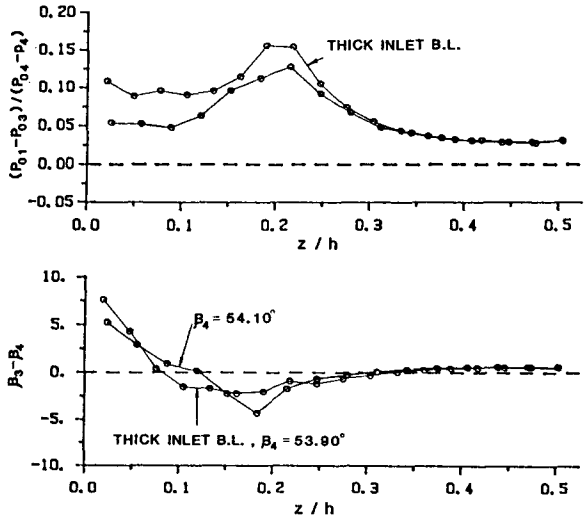


**Fig. 21 Mixed out pitchwise flow angle and stagnation pressure loss : inlet boundary layer thickness variation**

inlet vorticity. The mid-span loss is virtually unchanged. Table 4 shows that all of the apparent increase in stagnation pressure loss is due to the increased loss of the inlet boundary layer. Therefore, the production of new secondary loss is not necessarily linked with the magnitude of the inlet endwall boundary layer. The authors of references [9] and [10] made a similar observation.

## CONCLUSIONS

The performance of a linear cascade of low pressure turbine rotor hub profiles has been investigated over a range of parameters. It has been found that the production of new secondary loss increases with increasing Reynolds number, incidence and pitch-chord ratio. It was apparently independent of the nature of the incoming endwall boundary layer.

The development of the three-dimensional flow field, however, was not as straightforward as the above statement implies. For example, the interaction between the endwall flow and the suction surface separation bubble, when present, affected the number, position and size of the individual loss peaks. Under some but not all conditions, the centre of the passage vortex coincided with a loss peak. Furthermore, the strengths and positions of the passage and other vortices although largely independent of the Reynolds number, were clearly a function of the inlet boundary layer and of the blade loading, the latter being demonstrated by the changes in incidence and pitch-chord ratio.

Undoubtedly, the variation in both the net loss production and the character of the flow field caused by the performed changes in the flow conditions and geometry require further consideration. As well as the obvious and direct effect of secondary loss production upon machine performance, there exists the question of how the overall and the detailed structure of the exit flow from one blade row affects the performance of the next.

## ACKNOWLEDGMENT

The work described was supported by the Ministry of Defence and Rolls-Royce Limited. The assistance of their representatives, in particular Mr. C.T.J. Scrivener of Rolls-Royce and their permission to publish the work described in this paper, is gratefully acknowledged. The authors also wish to thank the members of the Whittle Laboratory for their assistance.

## REFERENCES

[1] Ainley, D.G., and Mathieson, G.C.R., "A method of performance estimation for axial flow turbines", A.R.C. R. & M. 2974, December 1951

[2] Balje, O.E., "Axial cascade technology and application to flow path designs, Part I", ASME Paper No. 68-GT-5, 1968

[3] Dunham, J., and Came, P.M. "Improvements to the Ainley-Mathieson method of turbine performance prediction" ASME Journal Eng. Power, Vol 92, 1970, pp252-256.

[4] Craig, H.R.M., and Cox, H.J.A., "Performance Estimation of Axial Flow Turbines", Proc. Inst. Mech. Eng. Vol. 1985, 1970-71, pp 407-424

[5] Hodson, H.P., and Dominy, R.G., "Three Dimensional Flow in a Low Pressure Turbine Cascade" To be presented

[6] Hodson, H.P., "Boundary Layer Transition and Separation near the Leading Edge of a High Speed Turbine Blade", ASME Jnl Eng. Gas Turbine and Power, Vol 107, Jan 1985, pp127-134

[7] Langston, L.S., "Crossflows in a Turbine Cascade Passage", ASME paper 80-GT-5, 1980

[8] Dunham, J., "A review of cascade data on secondary losses in Turbines", Jnl. Mech Eng. Sci., Vol. 12, No. 1, 1970, pp 48-58

[9] Marchal, P., and Sieverding, C.H. "Secondary Flows within Turbomachinery Bladings", Paper 11, AGARD Conference on "Secondary Flows in Turbomachines", AGARD CP-214, 1977

[10] Gregory-Smith, D.G., and Graves, C.P., "Secondary Flows and Losses in Axial Flow Turbines", ASME paper 82-GT-19, 1982.